HHS Public Access

Author manuscript

J Muscle Res Cell Motil. Author manuscript; available in PMC 2017 January 04.

Published in final edited form as:

J Muscle Res Cell Motil. 2015 December ; 36(6): 463–477. doi:10.1007/s10974-015-9440-2.

In Vitro and In Vivo Single Myosin Step-Sizes in Striated Muscle [a]

Thomas P. Burghardt[1,2,*], **Xiaojing Sun**[1], **Yihua Wang**[1], and **Katalin Ajtai**[1]

[1] Department of Biochemistry and Molecular Biology, Mayo Clinic Rochester, Rochester, MN 55905, USA

[2] Department of Physiology and Biomedical Engineering, Mayo Clinic Rochester, Rochester, MN 55905, USA

Abstract

Myosin in muscle transduces ATP free energy into the mechanical work of moving actin. It has a motor domain transducer containing ATP and actin binding sites, and, mechanical elements coupling motor impulse to the myosin filament backbone providing transduction/mechanical-coupling. The mechanical coupler is a lever-arm stabilized by bound essential and regulatory light chains. The lever-arm rotates cyclically to impel bound filamentous actin. Linear actin displacement due to lever-arm rotation is the myosin step-size. A high-throughput quantum dot labeled actin *in vitro* motility assay (Qdot assay) measures motor step-size in the context of an ensemble of actomyosin interactions. The ensemble context imposes a constant velocity constraint for myosins interacting with one actin filament. In a cardiac myosin producing multiple step-sizes, a "second characterization" is step-frequency that adjusts longer step-size to lower frequency maintaining a linear actin velocity identical to that from a shorter step-size and higher frequency actomyosin cycle. The step-frequency characteristic involves and integrates myosin enzyme kinetics, mechanical strain, and other ensemble affected characteristics. The high-throughput Qdot assay suits a new paradigm calling for wide surveillance of the vast number of disease or aging relevant myosin isoforms that contrasts with the alternative model calling for exhaustive research on a tiny subset myosin forms. The zebrafish embryo assay (Z assay) performs single myosin step-size and step-frequency assaying *in vivo* combining single myosin mechanical and whole muscle physiological characterizations in one model organism. The Qdot and Z assays cover "bottom-up" and "top-down" assaying of myosin characteristics.

Keywords

cardiac muscle myosin; *in vitro* motility; *in vivo* single myosin imaging; myosin step-frequency; myosin step-size; Qdot assay; second characterization; skeletal muscle myosin; zebrafish

Background

Myosin is the muscle energy transducer with an ATPase in a globular head domain called subfragment 1 (S1) and tail domain that forms myosin dimers and multimeric thick

[a]This work was supported by National Institutes of Health grant R01AR049277

[*]Corresponding author burghardt@mayo.edu.

filaments (**Fig 1**). Thick filaments interdigitate with actin thin filaments in striated muscle and slide relatively during contraction (Huxley 1969). S1 contains ATP and actin binding sites and a lever-arm whose rotary movement cyclically applies tension to move the load while myosin is strongly actin bound. The lever-arm converts torque generated in the motor into linear displacement (step-size) and undergoes shear strain that affects the lever-arm (**Fig 1** blue & black α-helix), the bound ELC (silver), and RLC (red). RLC stabilizes the lever-arm (Lowey et al. 1993; Pant et al. 2009; Sherwood et al. 2004) and RLC mutants implicated in disease lower velocity, force, and strain sensitivity (Greenberg et al. 2010) suggesting they alter lever-arm processing of shear stress. Similar significance is attributed to ELC (Wang et al. 2013a).

The standard *in vitro* motility assay measures actin gliding velocity over myosin immobilized on a surface. Myosin translates actin only while the two molecules are strongly bound. The myosin duty-ratio is the time spent strongly actin bound divided by the ATPase cycle time. Muscle myosin has low duty-ratio to enable rapid actin translation in a muscle fiber containing densely packed arrays of myosin motors (O'Connell et al. 2007). Low duty-ratio cardiac myosins elude conventional single molecule assays because actomyosin dissociates quickly and the freely moving element diffuses away prohibiting further interaction. Laser trapping solved the problem by confining the relevant molecules to a region small enough to ensure their repetitive interaction with high probability (Finer et al. 1994). We introduced super-resolution particle tracking of Qdot labeled actin to the standard *in vitro* motility assay (Qdot assay) (Wang et al. 2013b). The *in vitro* motility assay varies probability for actomyosin interaction with myosin surface density and actin filament length while actin diffusion is inhibited by methylcellulose in the motility buffer. The net effect sustains the actomyosin complex while preserving a subset of encounters that do not overlap in time on a single actin filament. The unitary myosin step is isolated in time and space then characterized using spatial super-resolution.

Mutations accompanying inheritable myopathies (IM's) frequently implicate S1. The large cost required to perform the single myosin mechanical characterization using a laser trap has limited attempts to a dozen or so IM heart disease linked mutants in S1 despite an inventory numbering in the several hundred (Moore et al. 2012). The latter has led to a persistent ambiguity between single myosin characteristics and IM phenotype. The Qdot assay records hundreds of single myosin unitary steps simultaneously in a single image using a standard research microscope setup vastly expanding assay capacity and availability (Wang et al. 2013b). The Qdot labeled single actin filaments translate in steps ranging from 3 to ~250 nm in the order caused by the actin filament microenvironment providing multiplexed time-distance data. The data is decoded in the event-velocity histogram with the low velocity end readily interpretable as single molecule step-sizes and step-frequencies.

Experimental preparations are identical to those for the ubiquitous *in vitro* motility assay except for the Qdot labeling of actin. The latter is one additional incubation step following preparation of the *in vitro* motility slide. Optimizing conditions for estimating step-size follows guidelines we developed usually requiring 2 or 3 measurement/analysis cycles to select parameters for exciting light intensity, time-resolution, and bulk concentration of motor protein (Wang et al. 2013b) . Once optimized, measurement consists of imaging the

movement of 40-80 Qdot labeled filaments in each of 2-3 slides for each condition or motor protein investigated. We typically do this measurement on three independent myosin preparations. The modern Qdot assay is massively-parallelized, high-throughput, and automated consistently achieving a step-assaying speed-up of ~1000 fold (to hours from months) compared to the standard approach. Statistical analysis of single myosin mechanical characterization is now meticulously managed by a vast data set consisting of thousands of single myosin mechanical events. The speed and accuracy of the method provides new opportunities to characterize related myosin isoforms in a heterogeneous mixture.

In complementary work, we use single myosin approaches to measure dynamics *in situ* and *in vivo*. C-terminus tagged human ventricular RLC (MYL2) with green fluorescent protein (RLC-GFP) was exchanged into permeabilized skeletal (Burghardt et al. 2007) or cardiac papillary muscle fibers (Burghardt et al. 2011). In both cases, recovery of isometric contraction from extensively and specifically exchanged myosin cross-bridges in the fibers implied the GFP did not deter muscle contraction. The photoactivatable GFP variant (PAGFP) C-terminus tagged RLC, RLC-PAGFP, was individually activated in the exchanged papillary muscle fibers isolating single myosin cross-bridges *in situ*. Single cross-bridge lever-arm orientation was measured at super-resolution from fibers in rigor, relaxation, and active isometric conditions. Single molecule orientation was also measured for the exchanged RLC-PAGFP modified by disease linked mutations to RLC (Burghardt and Sikkink 2013). The exchanged mutant RLC lowered lever-arm stiffness and impaired lever-arm transduction/mechanical-coupling. These disease linked mutants spanned the RLC structure and indicated position dependent change to lever-arm functionality. We adapted this single molecule technology to *in vivo* experimentation in zebrafish embryos (Sun et al. 2014).

The zebrafish embryo is transparent to visible and infrared light allowing unprecedented access for 3-dimensional imaging using wide field fluorescence microscopy with sheet (Huisken et al. 2004) or highly inclined thin (HILO) illumination (Tokunaga et al. 2008). The zebrafish sequenced genome indicates homologs for most protein coding human genes (Howe et al. 2013). Forward genetic screening identified fish mutants causing cardiac defects that provided insight into causes of inheritable human cardiac disease including dilated cardiomyopathy (DCM) (Xu et al. 2002) and cardiac valve defects (Hurlstone et al. 2003). The zebrafish has been increasingly used to model human cardiac disease in reverse genetic approaches due to zebrafish/human cardiac myosin structural (González-Solá et al. 2014) and disease phenotypes similarities (Bakkers 2011), and their applicability to high throughput screening methods (Burns et al. 2005). Zebrafish embryos are suited to muscle research because they develop externally, skeletal muscle comprises a large fraction of their body volume, and they begin to move very soon after gastrulation (Bassett and Currie 2003). The unc45b and cmlc2 promoters drive robust gene expression throughout zebrafish striated musculature (Berger and Currie 2013) and specifically in cardiac muscle (Huang et al. 2003), respectively. The zebrafish embryo model organism places the myosin transducer in its native context for experimentation. We explore active myosin dynamics using this new system for *in vivo*, single myosin, super-resolution imaging.

In Vitro Step-Size and Step-Frequency of Single Myosins in an Ensemble

Protein preparations

Porcine cardiac myosin (βmys) was prepared from porcine heart ventriculum as described (Ajtai et al. 2001; Wang et al. 2013b). Phosphorylated cardiac myosin was prepared using recombinant smooth muscle myosin light chain kinase (smMLCK) as described previously (Josephson et al. 2011). βmys with cleaved ventricular ELC (vELC, Δ17) was prepared using papain digestion as described previously but with modifications (Moczarska and Kakol 1995). Activated papain was added to 4 μM βmys solution in a mass ratio of myosin to papain of 90:1 or 180:1 in a buffer containing 100 mM NaCl, 10 mM imidazole pH 7.0, 4 mM $MgCl_2$, 1 mM DTT, 0.5 mM EGTA and 3 mM ATP. After 40 (90:1 myosin:papain ratio) or 16 (180:1) seconds at 23 °C, the reaction was stopped with 200 μg/ml leupeptin. ATP, papain, and most of the leupeptin were removed from the cleaved myosin by two myosin precipitations at low ionic strength as described (Wang et al. 2013b). Control βmys used in the assays was treated identically except for the treatment with papain.

All research conducted on mouse cardiac myosin was done in collaboration with Danuta Szczesna-Cordary (University of Miami, Miami, FL). Mouse cardiac myosin (αmys) was isolated from groups of mouse hearts including non-transgenic (NTg), transgenic mice expressing human vELC (WT), and transgenic mice expressing a 43 residue N-terminal truncated human vELC (Δ43) according to Kazmierczak et al. (Kazmierczak et al. 2009).

In vitro motility and Qdot assay

In all assays myosin is adsorbed to a nitrocellulose-coated-glass substrate exactly as described (Kron et al. 1991). We assume potential differences in nitrocellulose-coated-substrate/myosin interactions among the various isoforms tested had negligible implications for motility or Qdot assay results. Rhodamine labeling of actin filaments for the standard *in vitro* motility assay was performed with rhodamine-phalloidin and actin in a 1.2:1 molar ratio as described (Kron et al. 1991). Qdot assay uses Quantum dot 565 streptavidin conjugate (Qdot) binding biotin on biotin-XX-phalloidin (Life Technologies, Grand Island, NY) labeled actin filaments. Conditions favor an average of one Qdot per 1-2 μm long actin filament. Qdot streptavidin conjugation to the biotin-XX-phalloidin labeled actin was done in the motility flow cell all as described (Wang et al. 2013b). All *in vitro* assay experiments discussed have >90% of the actin filaments moving.

Qdot fluorescence from translating actin is imaged with through-the-objective total internal reflection fluorescence (TIRF) (Stout and Axelrod 1989) on an inverted microscope using a 150X, 1.45 NA objective (Qlympus, Center Valley, PA). TIRF illumination is evanescent and confined to within ~100 nm of the flow cell surface containing the immobilized myosin. Images were acquired with an EMCCD camera (Andor, Belfast, UK) at 60, 200, or 500 ms intervals indicated by Δt (depending on the actin sliding velocity), with exposure times of 12, 30, and 50 ms, and using Andor's SOLIS software. Intensity values were converted to photons using the conversion formula in SOLIS and the images output in TIFF format for reading into ImageJ. Argon ion laser (Coherent, Santa Clara, CA) intensity was ~30 mW at 488 nm.

We investigated *in vitro* actin velocities for rhodamine-phalloidin-labeled actin vs Qdot-labeled + rhodamine-phalloidin-labeled actin filaments. We found no significant motility velocity difference for the two labeled actin species when skeletal muscle heavy meromyosin (HMM) bulk concentration is ≥0.114 μM. Results are similar for βmys (Wang et al. 2013b).

In each assay a few Qdots do not move due to their immobilization on the flow cell surface. These particles are tracked at super-resolution to quantitate thermal/mechanical fluctuations.

High-throughput super-resolution measurements

We processed photon converted images for super-resolution using QuickPALM (Henriques et al. 2010). The software identifies and localizes point objects qualified for super-resolution fitting according to user specifications including minimum SNR (> 25 selects only Qdots) and maximum full width at half maximum (FWHM) of 5 pixels (107 nm/pixel in object space for the 150X objective). QuickPALM analysis produces a table (SRTable) listing each qualifying particle, particle position in pixels, position standard deviation, and frame identifier. Using the SRTable, QuickPALM renders the super-resolved particle data as single pixels per particle in the frame sequence of the original data. Super-resolved Qdot positions from each track in the rendered frames are linked in a time ordered sequence using our machine vision software QPTracklinker (Matlab) producing a list read by SRTrack (Mathematica). SRTrack updates the SRTable with the frame-to-frame tracking linked list eliminating any incorrectly identified particles that did not have a super-resolved equivalent. The latter removed the effect of Qdot blinking. Matlab and Mathematica programs are available from the authors.

Simulation

In vitro motility has myosin moving actin under unloaded conditions with a motility velocity s_m such that,

$$S_m = V_{\max}\frac{d}{f} \quad (1)$$

for the simplest case of myosin with one step-size d and duty-ratio f (O'Connell et al. 2007). Duty-ratio is the time actomyosin is strongly bound during an ATPase cycle, t_{on}, divided by the cycle time, $1/V_{max}$, hence,

$$t_{on} = \frac{f}{V_{\max}} \quad (2)$$

The t_{on} is distributed exponentially as observed for the actin detachment rate in the *in vitro* motility assay (Palmiter et al. 1999).

Muscle myosins produce multiple unitary steps with differing step-sizes necessitating introduction of the relative step-frequency, ω_j, for unitary step j (Wang et al. 2013b; Wang et al. 2014b). It is proportional to the rate of cross-bridge cycling with the higher rate producing a more frequent j th step. The dimensionless relative step-frequency is normalized

such that $\Sigma_j \omega_j = 1$. The absolute cycling rate for step j, V_j, has $V_j = V_{max} \omega_j$ and with $V_{max} = \Sigma_j V_j$.

In an ensemble of cross-bridges interacting with one actin filament, like the conditions in every muscle or motility assay, only one actin velocity is possible hence motility velocity s_m is the same for each unitary step-size implying each step-size has unique duty-ratio and time strongly actin bound. From eq. 1, step j duty-ratio,

$$f_j = \frac{d_j V_j}{S_m} = \frac{V_{\max}}{S_m} d_j \omega_j \quad (3)$$

and from eq. 2, the time myosin spends strongly bound to actin,

$$t_{on,j} = \frac{1}{S_m} d_j \omega_j \quad (4)$$

Qdot velocities are plotted in velocity-event histograms covering the low velocity domain of 0~4 natural velocity units (vu) where $(d_I/\Delta t) = 1$ for d_I a suitable and dominant intermediate step-size and frame capture interval Δt. Eq. 4 affects how we simulate the velocity-event histogram since each unitary step has a unique t_{on} that varies with step-size and relative step-frequency. **Fig 2** shows a time course for an actin filament over a time interval of $3\Delta t$'s (from t = 0 to $3\Delta t$) containing 4 hypothetical actomyosin interactions. The motor performs 3, 5, or 8 nm unitary steps using different lever-arm movements. Column vectors explicitly indicate the time course with t_{on} the time strongly actin bound. Two myosins simultaneously strongly bind actin in the second Δt where displacement is unlike the canonical 3, 5, or 8 nm steps due to overlap of strong actin binding states. The latter causes the rising baseline in the event-velocity histogram because some actin filaments move at velocities that are not quantized but rather forming a continuum of values.

V_{max} and average motility velocity, s_m, are measured under saturating actin and myosin conditions, respectively. They are constant parameter inputs to the simulation that are characteristic to each myosin tested. The unknown parameter set actively searched in the simulation consists of the actin binding probability for myosin (1 free parameter), step-size (n free parameters for n unitary step-sizes), and relative step-frequency (n-1 free parameters due to normalization). Trial parameter values are generated in the simulation by random choice from a range of values set at the start of the simulation. Peak position and area, usually from the first n peaks in the velocity-event histogram, are the unitary step-size and relative step-frequency estimates obtained directly by inspection. Estimates for step-size and step-frequency from simulation rigorously account for step overlap when two or more myosins impinge on one actin filament during some of the time they are strongly actin bound.

A typical high-throughput Qdot assay data set consists of 10-12 acquisitions (one acquisition is one *in vitro* motility movie) from a preparation of one unknown and one control protein. Three separate protein preparations give a total of 30-36 acquisitions for each protein isoform. Total events acquired in the velocity unit range typically sampled have increased by an order of magnitude over previous applications by using the high-throughput methods.

Simulation of the pooled data set requires a similar increase in computing cost. We have changed to a fixed computing cost basis by simulating a standard event total for the event-velocity histogram that is renormalize to match event total in each acquisition. Comparison to data minimizes the χ^2 goodness-of-fit test that is weighted by event total then summed over all the acquisitions for evaluating global goodness-of-fit.

Simulated data ensembles are created by using the 30-36 best fitting event-velocity histogram simulations generated. These event-velocity simulations are combined linearly to approximate the measured event-velocity histogram with coefficients ≥0 and summing to 1 (ensuring event count is conserved) while minimizing the χ^2 goodness-of-fit test with all points equally weighted. Simulation results are reported in the fitted event-velocity histogram and the simulation count/step-frequency histogram indicating the normalized distribution of step-frequency for each step with red indicating short, green for intermediate, and blue for long steps.

Systemic (ensemble) analytics

System analytics for the multi-step motor and step-frequency weighted averaged quantities indicated with < > were derived previously (Wang et al. 2014a). They define the average step-size <d>, average force <F> proportional to the duty–ratio or fraction of strongly actin bound cross-bridges (eq. 3) (Gordon et al. 1966), and average power <P> = S_m <F> such that,

$$<d>=\sum_j \omega_j \cdot d_j \quad \text{and} \quad <F>=\alpha\sum_j \omega_j \cdot f_j \quad (5)$$

for α the proportionality constant expressed in units of force (uf) where α=1.

Statistics

Three or more different myosin preparations generate independent data sets for the step-size/step-frequency experiments. Step-size and step-frequency findings from simulation are compared using one-way ANOVA with Bonferroni or Tukey post-tests for significance at the 0.05 level.

Natural Myosin Activation

The Qdot assay performed on rabbit skeletal HMM (sHMM) indicated a dominant ~5 nm step-size as expected for this isoform (Steffen et al. 2001). βmys indicated three unitary steps-sizes of ~3, ~5, and ~8 nm with 5 nm the major contributor, 8 nm slightly less likely, and 3 nm a low probability step (Wang et al. 2013b). We proposed the model in **Fig 3** where the major 5 nm step is the default step identical to the unitary step in sHMM. The 8 nm step is different from the 5 nm step by involving an extra interaction with actin via the unique N-terminus of the cardiac ELC (cELC) (Lossie et al. 2014; Miller et al. 2005; Miyanishi et al. 2002; Muthu et al. 2011; Petzhold et al. 2014; Schaub et al. 1998; Timson 2003). The minor 3 nm step is the unlikely conversion of the 5 nm step to the full cELC bound 8 nm step. It occurs in just 1 of 8 cycles and is isolated in time from the 5 nm step by slow ADP

dissociation hence we sometimes observe it as a separate step (Siemankowski and White 1984).

Changes to the phosphorylation level of Ser15 in ventricular RLC in the cardiac muscle affect power output in model organisms (Miller et al. 2011; Scruggs and Solaro 2011). We investigated if RLC phosphorylation affects the unitary step-size/step-frequency using the Qdot assay. RLC in βmys was specifically phosphorylated at S15 (pRLC) using a smooth muscle myosin light chain kinase (smMLCK) (Josephson et al. 2011). Fractional phosphorylation levels of 0, 40%, and 85% (maximally phosphorylated) were investigated. We found that phosphorylation causes a dramatic re-distribution of step-frequencies (Wang et al. 2014b). These data are summarized in **Table 1** for the 0 (native) and 85% phosphorylated βmys (pβmys).

Table 1 indicates the actin-activated ATPase V_{max}, motility velocity, numerical values for the step-sizes and step-frequencies, and the ensemble averaged step-size, force and power of control (βmys) and 85% phosphorylated βmys (pβmys). The long step-frequency increases >2 fold, the intermediate step-frequency decreases 4 fold, and the short step-frequency is unchanged due to phosphorylation. The long and intermediate step-frequency changes due to phosphorylation are significant. Step-frequency re-distribution affects the mean step-size (eq. 5) causing an increase from ~5.3 nm to 6.2 nm with the RLC phosphorylation.

Modest changes to V_{max} and step-sizes coupled to the dramatic re-distribution of step-frequencies drives the higher force and power in the pβmys implying that S15 phosphorylation is the natural myosin activator. Higher RLC phosphorylation levels correlate with higher isometric force and power output in permeabilized rat cardiac trabeculae and with heart failure in human tissue (Toepfer et al. 2013) implying it is a compensation mechanism for power shortage in failing heart.

Pharmaceutical myosin activation

A selective pharmaceutical βmys activator, omecamtive mecarbil (OM), up-regulates cardiac contractility in vivo and is undergoing testing for heart failure therapy (Bakkehaug et al. 2015). *In vitro* βmys actin-activated ATPase, motility velocity, step-size, and step-frequency were measured to explore OM's effect on the single myosin characteristics of the motor operating in an ensemble. OM decreases motility velocity nearly 10 fold indicating a large increase in duty-ratio converting βmys to a near processive myosin. The Qdot assay in this application has labeled actin translating over surface bound porcine βmys at 0.16 μM bulk protein concentration in the absence and presence of 1.5 μM OM with 1% DMSO. DMSO is needed to increase the solubility of the OM in aqueous buffer but does not significantly impact βmys characteristics in motility and actin-activated myosin ATPase assays (Wang et al. 2014a).

Fig 4, Panels a & c show actin sliding event-velocity histograms in the low velocity domain 0-15 nm per unit time for Δt the 200 or 500 msec frame capture interval in the absence or presence of OM, respectively (Wang et al. 2014a). Baselines due to thermal/mechanical fluctuations were subtracted as described (Wang et al. 2013b). Measured (filled squares and dashed line) and simulated (red line) data are shown for the velocity curve. Peaks at the

lowest velocity range in **Fig 4** correspond to short (red), intermediate (green), and long (blue) step-sizes.

Fig 4, Panels b & d show the count/step-frequency histograms indicating step-frequency distributions and numerical averages ± standard deviation (SD) for the ~3, ~5, and ~8 nm unitary steps. Numerical average relative step-frequencies for control βmys are identical to within error to previously reported values where the 5 nm step-size is predominant (Wang et al. 2013b). In the presence of 1.5 μM OM, the 5 and 8 nm steps are equally frequent and the short step frequency is nearly unchanged. Step-size and step-frequency estimates and their standard error are summarized in **Table 1**. OM causes a large increase in ensemble force (<F> in eq. 5).

We explore implications of the dramatic rise in <F> for the OM treated βmys in the context of its three unitary step-sizes with comparison of native (βmys), pβmys, and OM+βmys movers in **Table 1**. The relative step-frequencies shift away from the intermediate step-size dominant in native βmys to the long step in phosphorylated and OM treated βmys. The shift is accompanied by rising <F> that is incremental or dramatic for pβmys or OM+βmys, respectively. <P> follows a different trend. Average power doubles for pβmys while slightly increasing for OM+βmys relative to native βmys. Both activators cause native cross-bridges to develop more force and power. System analytics indicate in **Table 1** that native βmys is optimized for peak speed and that the natural activator holds speed nearly constant while increasing <F> and <P> by increasing ω_L, the step-frequency for the long step. In contrast, OM treatment sacrifices speed for <F> by increasing the duty-ratio however this places an upper limit on relative frequencies because strong binding stabilization inhibits faster cycling. βmys phosphorylation is a natural nonlinear mechanism to adjust force-velocity in the cardiac muscle. βmys phosphorylation at RLC is a heart failure therapy target that has already been recognized (Mendes-Ferreira et al. 2013).

A model for in vitro step-size adaptation

We proposed the model in **Fig 3** as the basis for the three unitary steps in βmys. We tested the model using several constructs: a 17 residue N-terminal truncated cELC in porcine βmys (Δ17) made by papain digestion (Moczarska and Kakol 1995), and, a 43 residue N-terminal truncated human vELC expressed in a transgenic mouse heart (Δ43) (Kazmierczak et al. 2009). Control porcine and mouse cardiac myosin constructs have wild type porcine cELC on porcine myosin (Δ0), expressed native human cELC on mouse cardiac myosin (WT), and the nontransgenic mouse cardiac myosin (NTg). Mouse cardiac myosin has the α heavy chain (αmys). We measured myosin actin-activated ATPase, motility velocity, step-size, and step-frequency for all the isoforms (Wang et al. 2015).

Fig 5 Panels a & c show the Qdot assay velocity-event histogram for two βmys constructs in the low velocity domain of 0~3 velocity units and with frame capture interval $\Delta t = 0.2$ s. Baselines due to thermal/mechanical fluctuations were subtracted as described (Wang et al. 2013b). Measured (↑ connected with dashed line) and simulated (solid line) data are shown for the velocity-event curves. Peaks or inflection points appearing below 2 velocity units correspond to unitary short (↑ red), intermediate (↓ green), and long (↑ blue) step-sizes in nm. Intermediate and long steps in combination are also shown. The principal basis for

accurate simulation is identifying positions and probabilities for the 5 step-types ($\uparrow,\downarrow,\uparrow_L,\downarrow\downarrow,\downarrow\uparrow_L$) where $\uparrow_L$ means the long step. Step-size values for Δ0 βmys are equivalent to previous results (Wang et al. 2013b; Wang et al. 2014b) and statistically identical to Δ17 βmys. **Panels b & d** show the step-frequency simulation-count histograms. Numerical average step-frequencies ($\omega_S,\omega_I,\omega_L$) for control Δ0 βmys are identical to those reported previously (Wang et al. 2013b). Probability for the 5 nm step, ω_I, significantly increased while probability for the 8 nm step, ω_L, significantly decreased in Δ17 compared to control (one-way ANOVA). Probability for the 3 nm step, ω_S, is not detectably changed. We find that truncation of the cELC N-terminus in βmys down regulates cELC/actin binding resulting in these changes in step-frequency. Results for the mouse myosin constructs closely follow those for the βmys.

The truncation of the cELC N-terminus in β- and αmys down regulates cELC/actin binding supporting the **Fig 3** model. Our findings provide the structural mechanism for cELC regulation of transduction-mechanical coupling in muscle. It is a new and unexplored basis for modulating power generation by step-size adaptation.

Results obtained with the Qdot assay indicate how RLC phosphorylation and cELC N-terminus actin binding adapt the cardiac myosin unitary step-size. They identify and clarify two new and specific mechanisms for modulating power generation in cardiac muscle. Power generation with wide dynamic range is a key characteristic of a healthy heart that is constrained by heart failure disease. We can now shape our efforts in protein engineering, drug development, and other therapies towards intervention using these promising new mechanisms. Our investigations were made feasible mainly due to the speed and accuracy of the automated Qdot assay that lowers myosin unitary step assaying cost 1000 fold by thoughtful application of super-resolution microscopy, machine vision, and graphical processing unit (GPU) computing in simulation.

We detected 3 near-constant myosin step-sizes corresponding nominally to 3, 5, and 8 nm while distinguishing several myosin isoforms by their characteristic step-frequencies. An alternative model has 3 microdomains on the surface that adsorb myosin and impose these 3, 5, and 8 nm step-sizes (the 3 step-size microdomain model) that is based on evidence suggesting that a functionalized (but not nitrocellulose coated) surface adsorbed myosin skeletal HMM has heterogeneous (modeled as 3 but probably more) rates of a myosin ATPase (step-size was not measured) (Balaz et al. 2007). In this alternative model, changing step-frequencies observed with phosphorylation, OM binding, or the truncated version of the vELC are due to the different affinities these isoforms have for the 3 step-size microdomains.

Contradicting the 3 step-size microdomain model, preliminary *in vitro* force measurements using βmys and an α-actinin coated nitrocellulose surface have statistically identical myosin dimer step-sizes and step-frequencies as the plain nitrocellulose only surface. Experiments in the presence of OM (discussed here) receive the drug after myosin is surface adsorbed (presumably precluding adsorbed myosin from changing from one microdomain to another) yet step-frequency is altered (**Fig 4**). A laser trapping experiment reported 2 myosin step-sizes of 5 and 9 nm from native mouse cardiac ventricular myosin with step-frequency in

approximate agreement with our values independently implying step-sizes and step-frequencies are an intrinsic myosin property (Tyska et al. 2000). Tyska et al. propose that the two step-sizes are due to the two heads in a myosin dimer. We propose that the low-frequency 3 nm step was unnoticed and the presence of the steps at 5 and 9 nm is the effect of the cardiac ELC N-terminus binding to actin from our model in **Fig 3**.

Single Myosins *In Vivo*.

Sample preparation—We co-injected transposase mRNA and plasmid containing a Tol2 construct with the zebrafish unc45b enhancer (Berger and Currie 2013) and the gene for RLC-GFP or RLC-PAGFP into the cytoplasm of one-cell-stage embryos (Higashijima et al. 1997; Kwan et al. 2007). unc45b enhancer drives RLC-GFP or RLC-PAGFP expression in zebrafish musculature including skeletal muscle (Berger and Currie 2013). Usually ~300-500 embryos were injected. Embryos were maintained in petri dishes in zebrafish water (stock solution of 300 mM NaCl, 10 mM KCl, 20 mM $CaCl_2$ and 20 mM $MgSO_4$ diluted 1:60 stock:H_20) at 28 °C. At 21-25 somites stage, the embryos were treated with 0.5 mM 1-phenyl 2-thiourea (PTU) to inhibit melanogenesis. At 2-3 days post-fertilization (2-3 dpf), we screened embryos for green fluorescence excited by 488 or 405 nm (GFP or PAGFP) transmitted light using a 10X objective. The selected embryos had their chorion removed. At 3-4 dpf the embryos were anesthetized in 0.16 mg/ml tricaine for experimentation. Zebrafish were handled in accordance with IACUC guidelines in an approved protocol (A47113).

Microscopy—Individual zebrafish embryos were confined in an aqueous buffer droplet then placed into a 200 μm deep, 3 mm wide, and 10 mm long microfluidic channel with the channel side up. The device with embryo was inverted then placed on top of a #0 glass coverslip forming a water tight seal with the glass as shown in **Fig 6 panels a & b**. The view in **panel b** from the top is through the actual device. Inlet/outlet holes through the microfluidic substrate (polydimethylsiloxane or PDMS) allowed solution to be exchanged as needed using a 20 μL pipette. Channel size confined the embryo to lie flat although tail flipping movement was observed. Embryos lived for hours under continuous observation. Fluorescence or reflected second harmonic generation (SHG) was observed in an inverted wide field microscope under HILO illumination through the glass coverslip or in an upright scanning microscope through the PDMS, respectively. The HILO beam from an oil immersion, 100X, 1.3 NA objective is visualized in **Fig 6 Panel c**. The PDMS cube doped with rhodamine B creates a cavity on top of the coverslip. The beam leaves the glass coverslip at the bottom and propagates through an aqueous solution containing fluorescein imitating the fish medium in a fish confinement microfluidic channel. Emergent beam angle of 74 deg results from an incident angle of ~57.7 deg.

Fig 7 overlays simultaneously collected 2-photon (2-P) images using 810 nm infrared light exciting fluorescence at ~500 nm (green) and SHG at 405 nm (blue) in a RLC-GFP tagged embryo. A 20X, 1.0 NA water immersion objective has a 2 mm working distance to image the embryo through the microfluidic. Shown are a wide view of the trunk skeletal muscles in the tail (*left*) and a close-up of two single fibers (*right*). SHG originates exclusively from the myosin in the A-band (Plotnikov et al. 2006). The M-line separates the opposing myosin

dimers in the thick filament. The I-band contains the actin thin filament. M-lines are separated by ~2.1 μm. The single fiber image demonstrates that the fluorescence and SHG exactly co-localize indicating the tag labels the myosin lever-arm as demonstrated previously in rabbit skeletal and porcine cardiac permeabilized muscle fibers (Burghardt et al. 2007; Burghardt et al. 2011).

Fig 8 compares RLC-PAGFP (top) to RLC-GFP (bottom) tagged embryos under HILO illumination at 488 nm excitation. A 100X, 1.3 NA oil immersion objective has 200 μm working distance that can image the sample anywhere in the microfluidic chamber. The HILO beam propagating at 74° to the microscope optical axis has ~4 μm illumination depth. Narrower depths down to ~1 μm are achievable by reducing beam diameter giving a smaller illuminated field. The RLC-PAGFP tagged sample shows several instances of photoactivated chromohores over a background of weakly fluorescing unphotoactivated RLC-PAGFP. Images were 1 sec exposures recorded over 1 min (60 exposures in a record). We identified single molecule events with quantized activation over background intensity or quantized photobleaching back to background from the points of light appearing in the image over time (Sun et al. 2014).

Single myosin analytics—Single molecule intensity patterns from zebrafish embryo skeletal muscle myosins in relaxation were fitted using the pattern recognition algorithm and subjected to orientation super-resolution analysis (Bobroff 1986; Burghardt 2011). The intensity patterns determine the emission dipole moment coordinates (β',α') for β' the spherical polar angle and α' the azimuth in muscle fiber coordinates where the z-axis is parallel to the fiber symmetry axis, x-axis is in the plane of the coverslip, and y-axis is normal to the coverslip plane pointing into the aqueous medium [details in (Burghardt 2011; Burghardt et al. 2011; Burghardt and Sikkink 2013)]. **Fig 9 panels a & b** shows *in vivo* single myosin data from relaxed skeletal zebrafish embryo muscle (open black triangles). Single moieties were photoactivated with either p- or s-polarized exciting light (e_p or e_s) polarized in the x-y plane or z-axis. The (β',α') coordinates indicate that extremes, 0 and 180 deg for either α' or β' and in the central region where (β',α') ≈ (90,90), are unpopulated due to steric/crowding forces originating from the thick filament. Steric/crowding forces are not replicated in vitro (Burghardt et al. 2011).

S1/GFP coordination—We estimated (PA)GFP moiety coordination with the myosin lever-arm in RLC-(PA)GFP tagged myosin. The method chooses best agreement between simulated S1/GFP complexes generated using ZDOCK (Pierce et al. 2011) and experimental data measuring (β',α') in **Fig 9** converted to S1/GFP coordination trials using, crystal structures of S1 (Rayment et al. 1993) and GFP (Brejc et al. 1997), chromophore dipole orientation in the GFP crystal structure (Rosell and Boxer 2003), and the expected relationship between myosin in opposite half-sarcomeres in the muscle fibers. This process selected several S1/GFP coordinations simultaneously satisfying all constraints. Final refinement favored the S1/GFP docking indicated in **Fig 1**. The S1 structure in **Fig 1** is that of human β-cardiac myosin (βS1) from the homology modeling (Marti-Renom et al. 2000) of its sequence using the chicken skeletal myosin S1 crystal structure 2mys (Rayment et al. 1993). The myosin lever-arm orientation is defined by the symmetry axis of its α-helix at

the RLC binding site shown in black. The simulated (β',α') data are practically indistinguishable from the experimental data shown in **Fig 9**. The (β,α) data (open blue squares) refers to lever-arm orientation. The rigidity of the S1/GFP coordination for skeletal and cardiac isoforms was also demonstrated (Sun et al. 2014).

Single relaxed skeletal myosin lever-arms in live zebrafish embryos were imaged and analyzed with orientation super-resolution for the first time using a photoactivatable tag on a myosin light chain expressed in the embryo (Sun et al. 2014). Tag specificity was demonstrated by the simultaneous observation of 2-P fluorescence and SHG signals from the muscle (**Fig 7**). Single molecule detection was achieved using wide field HILO illumination and verified by observing quantized photoactivation and photobleaching. Single molecule emission patterns were subjected to orientation super-resolution analysis. They indicated a highly orientationally confined myosin lever-arm orientation distribution shown in **Fig 9**.

Single Myosin Lever-Arm Orientation in Active Zebrafish Embryo Muscle

Active skeletal muscle

An "accordion" phenotype in a zebrafish embryo is attributed to the simultaneous contraction of the bilateral tail muscles with treatment by strychnine (Hirata et al. 2005). The effect is attributed to strychnine blocking of the inhibitory glycine receptor (GlyR). In humans, strychnine also blocks GlyR and causes skeletal muscle stiffness because the muscle cannot relax for an extended period following spasm. We developed a protocol to induce isometric skeletal muscle contraction in embryos. A 10 mM stock strychnine solution was made fresh daily. Two 3 dpf embryos tagged with RLC-PAGFP were placed in separate 200 μm deep microfluidic channels (on one chip) in 20 μL of 30% Danieau Buffer (D-buffer, 17.4 mM NaCl, 0.21 mM KCl, 0.12 mM $MgSO_4$, 0.18 mM $Ca(NO_3)_2$, 1.5 mM HEPES, pH 7.6). Embryos were stimulated by touching with forceps to elicit a robust escape reflex consisting of a short burst of tail strokes for swimming (touch-test). We introduced 10 or 70 μM strychnine to the buffer of one embryo and tested the escape reflex at short time intervals thereafter. In 15 or 5 min the strychnine treated embryo did not respond to the touch-test but displayed a "shivering" movement suggesting apparent extended bilateral contraction in the tail muscles. No effect was observed on heart rate or blood circulation. Both embryos (relaxed control and strychnine treated) were imaged at a 1 Hz frame rate for single myosin orientation super-resolution measurements using HILO with p-polarized photoactivation. Following the imaging session of ~20 min, the embryos were rinsed three times in D-buffer and returned to separate 60 mm petri dishes containing 10 ml of D-buffer. The 10 or 70 μM strychnine treated embryos recovered normal touch-test response in 5-10 min or overnight, respectively.

Single myosin orientation super-resolution measurements from the photoactivated RLC-PAGFP tagged myosin lever-arms in active isometric muscle were made just as described for relaxed muscle (Sun et al. 2014). **Fig 9 panel c** shows dipole (open black triangles) and lever-arm orientation (open blue squares) in the active isometric muscle. They exhibit much wider dispersion in both β' and α' degrees of freedom than the relaxed muscle. The 10 μM strychnine treated embryos have lever-arm distribution intermediate between those shown in

panels a & c indicating a dose response. Control relaxed embryos, and recovered embryos relaxed after the strychnine treatment, gave results identical to those in **panel a**.

Super-resolved orientation of photoactivated RLC-PAGFP emission dipoles were computed from images continuously recorded for ~2 min from zebrafish skeletal muscle in active isometric conditions. The time-resolved coordinates have probe dipole or lever-arm helix spherical polar angles (β',α') or (β,α) defined relative to a fiber fixed frame. They are the trajectories for a single dipole or lever-arm. The arc subtended by a single lever-arm helix as it rotates in sequential images defines a sequence of chords on a circle of diameter equal to the lever-arm length. Chord length is a myosin unitary step-size when the frame sequence captures the power stroke. These experiments currently challenge us.

Conclusion

The massively-parallel and high-throughput automated Qdot assay is now in use. It speeds up myosin unitary step-assaying 10^3 fold compared to the standard method and represents a unique innovation and opportunity. It enables the dramatic expansion of unitary step-assaying coverage to interesting myosin variants. The unprecedented coverage will contribute substantively to the informatics for myosin structure/function *in vitro*.

Single myosin detection provides the "bottom-up" myosin characterization probing basic transduction/mechanical coupling mechanisms in myosin without ambiguities inherent to ensemble observation. Macroscopic muscle physiological experimentation provides the definitive "top-down" phenotype characterizations that are the concerns in translational medicine. *In vivo* single myosin detection in muscle from zebrafish embryo models for human muscle fulfill ambitions for both bottom-up and top-down experimentation in the native environment. It delineates *in vitro* and *in vivo* myosin complementarity that is critically important for exploring mechanisms for how drugs, mutations, or post translational modifications impact myosin in muscle contraction.

REFERENCES

Ajtai K, Garamszegi SP, Park S, Velazquez Dones AL, Burghardt TP. Structural characterization of β-cardiac myosin subfragment 1 in solution. Biochemistry. 2001; 40:12078–12093. [PubMed: 11580283]

Bakkehaug JP, et al. The Myosin Activator Omecamtiv Mecarbil Increases Myocardial Oxygen Consumption and Impairs Cardiac Efficiency Mediated by Resting. Myosin ATPase Activity Circulation: Heart Failure. 2015 doi:10.1161/circheartfailure.114.002152.

Bakkers J. Zebrafish as a model to study cardiac development and human cardiac disease. Cardiovasc Res. 2011; 91:279–288. doi:10.1093/cvr/cvr098. [PubMed: 21602174]

Balaz M, Sundberg M, Persson M, Kvassman J, Månsson A. Effects of Surface Adsorption on Catalytic Activity of Heavy Meromyosin Studied Using a Fluorescent ATP Analogue†. Biochemistry. 2007; 46:7233–7251. doi:10.1021/bi700211u. [PubMed: 17523677]

Bassett DI, Currie PD. The zebrafish as a model for muscular dystrophy and congenital myopathy. Hum Mol Genet. 2003; 12:R265–R270. doi:10.1093/hmg/ddg279. [PubMed: 14504264]

Berger J, Currie PD. 503unc, a small and muscle-specific zebrafish promoter. Genesis. 2013; 51:443–447. doi:10.1002/dvg.22385. [PubMed: 23444339]

Bobroff N. Position measurement with a resolution and noise-limited instrument. Rev Sci Instrum. 1986; 57:1152–1157.

Brejc K, Sixma TK, Kitts PA, Kain SR, Tsien RY, Ormo M, Remington SJ. Structural basis for dual excitation and photoisomerization of the Aequorea victoria green fluorescent protein. Proc Natl Acad Sci USA. 1997; 94:2306–2311. [PubMed: 9122190]

Burghardt TP. Single molecule fluorescence image patterns linked to dipole orientation and axial position: Application to myosin cross-bridges in muscle fibers. Plos One. 2011; 6:e16772. [PubMed: 21347442]

Burghardt TP, Ajtai K, Chan DK, Halstead MF, Li J, Zheng Y. GFP tagged regulatory light chain monitors single myosin lever-arm orientation in a muscle fiber. Biophys J. 2007; 93:2226–2239. [PubMed: 17513376]

Burghardt TP, Josephson MP, Ajtai K. Single myosin cross-bridge orientation in cardiac papillary muscle detects lever-arm shear strain in transduction. Biochemistry. 2011; 50:7809–7821. [PubMed: 21819137]

Burghardt TP, Sikkink LA. Regulatory light chain mutants linked to heart disease modify the cardiac myosin lever-arm. Biochemistry. 2013; 52:1249–1259. doi:DOI: 10.1021/bi301500d. [PubMed: 23343568]

Burns CG, Milan DJ, Grande EJ, Rottbauer W, MacRae CA, Fishman MC. High-throughput assay for small molecules that modulate zebrafish embryonic heart rate. Nat Chem Biol. 2005; 1:263–264. doi:http://www.nature.com/nchembio/journal/v1/n5/suppinfo/nchembio732_S1.html. [PubMed: 16408054]

Finer JT, Simmons RM, Spudich JA. Single myosin molecule mechanics: piconewton forces and nanometre steps. Nature. 1994; 368:113–119. [PubMed: 8139653]

González-Solá M, Al-Khayat Hind A, Behra M, Kensler Robert W. Zebrafish Cardiac Muscle Thick Filaments: Isolation Technique and Three-Dimensional. Structure Biophys J. 2014; 106:1671–1680. doi:10.1016/j.bpj.2014.01.050. [PubMed: 24739166]

Gordon AM, Huxley AF, Julian FJ. The variation in isometric tension with sarcomere length in vertebrate muscle fibres. J Physiol (Lond). 1966; 184:170–192. [PubMed: 5921536]

Greenberg MJ, Kazimierczak K, Szczesna-Cordary D, Moore JR. Cardiomyopathy-linked myosin regulatory light chain mutations disrupt myosin strain-dependent biochemistry. Proc Natl Acad Sci USA. 2010; 107:17403–17408. [PubMed: 20855589]

Henriques R, Lelek M, Fornasiero EF, Valtorta F, Zimmer C, Mhlanga MM. QuickPALM: 3D real-time photoactivation nanoscopy image processing in Image. J Nature Methods. 2010; 7:339–340.

Higashijima, S-i; Okamoto, H.; Ueno, N.; Hotta, Y.; Eguchi, G. High-Frequency Generation of Transgenic Zebrafish Which Reliably Express GFP in Whole Muscles or the Whole Body by Using Promoters of Zebrafish Origin. Dev Biol. 1997; 192:289–299. doi:http://dx.doi.org/10.1006/dbio.1997.8779. [PubMed: 9441668]

Hirata H, Saint-Amant L, Downes GB, Cui WW, Zhou W, Granato M, Kuwada JY. Zebrafish bandoneon mutants display behavioral defects due to a mutation in the glycine receptor β-subunit. Proc Natl Acad Sci USA. 2005; 102:8345–8350. doi:10.1073/pnas.0500862102. [PubMed: 15928085]

Howe K, et al. The zebrafish reference genome sequence and its relationship to the human genome. Nature. 2013; 496:498–503. doi:10.1038/nature12111 http://www.nature.com/nature/journal/vaop/ncurrent/abs/nature12111.html#supplementary-information. [PubMed: 23594743]

Huang C-J, Tu C-T, Hsiao C-D, Hsieh F-J, Tsai H-J. Germ-line transmission of a myocardium-specific GFP transgene reveals critical regulatory elements in the cardiac myosin light chain 2 promoter of zebrafish. Dev Dyn. 2003; 228:30–40. doi:10.1002/dvdy.10356. [PubMed: 12950077]

Huisken J, Swoger J, Bene FD, Wittbrodt J, Stelzer EHK. Optical sectioning deep inside live embryos by selective plane illumination microscopy. Science. 2004; 305:1007–1009. [PubMed: 15310904]

Hurlstone AFL, et al. The Wnt/[beta]-catenin pathway regulates cardiac valve formation. Nature. 2003; 425:633–637. doi:http://www.nature.com/nature/journal/v425/n6958/suppinfo/nature02028_S1.html. [PubMed: 14534590]

Huxley HE. The mechanism of muscular contraction. Science. 1969; 164:1356–1366. [PubMed: 4181952]

Josephson MP, Sikkink LA, Penheiter AR, Burghardt TP, Ajtai K. Smooth muscle myosin light chain kinase efficiently phosphorylates serine 15 of cardiac myosin regulatory light chain. Biochem Biophys Res Commun. 2011; 416:367–371. [PubMed: 22120626]

Kazmierczak K, Xu YY, Jones M, Guzman G, Hernandez OM, Kerrick WGL, Szczesna-Cordary D. The role of the N-terminus of the myosin essential light chain in cardiac muscle contraction. J Mol Biol. 2009; 387:706–725. [PubMed: 19361417]

Kron SJ, Toyoshima YY, Uyeda TQP, Spudich JA. Assays for actin sliding movement over myosin-coated surfaces. Methods Enzymol. 1991; 196:399–416. [PubMed: 2034132]

Kwan KM, et al. The Tol2kit: A multisite gateway-based construction kit for Tol2 transposon transgenesis constructs. Dev Dyn. 2007; 236:3088–3099. doi:10.1002/dvdy.21343. [PubMed: 17937395]

Lossie J, et al. Molecular mechanism regulating myosin and cardiac functions by ELC Biochem Biophys. Res Commun. 2014; 450:464–469. doi:http://dx.doi.org/10.1016/j.bbrc.2014.05.142.

Lowey S, Waller GS, Trybus KM. Function of skeletal muscle myosin heavy and light chain isoforms by an in vitro motility assay. J Biol Chem. 1993; 268:20414–20418. [PubMed: 8376398]

Marti-Renom MA, Stuart AC, Fiser A, Sanchez R, Melo F, Sali A. Comparative protein structure modeling of genes and genomes. Annu Rev Biophys Biomol Struct. 2000; 29:291–325. [PubMed: 10940251]

Mendes-Ferreira P, De Keulenaer GW, Leite-Moreira AF, Brás-Silva C. Therapeutic potential of neuregulin-1 in cardiovascular disease. Drug Discovery Today. 2013; 18:836–842. doi:http://dx.doi.org/10.1016/j.drudis.2013.01.010. [PubMed: 23384772]

Miller Mark S, Farman Gerrie P, Braddock Joan M, Soto-Adames Felipe N, Irving Thomas C, Vigoreaux Jim O, Maughan David W. Regulatory Light Chain Phosphorylation and N-Terminal Extension Increase Cross-Bridge Binding and Power Output in Drosophila at In Vivo Myofilament Lattice Spacing. Biophys J. 2011; 100:1737–1746. doi:http://dx.doi.org/10.1016/j.bpj.2011.02.028. [PubMed: 21463587]

Miller MS, et al. The essential light chain N-terminal extension alters force and fiber kinetics in mouse cardiac muscle. J Biol Chem. 2005; 280:34427–34434. [PubMed: 16085933]

Miyanishi T, Ishikawa T, Hayashibara T, Maita T, Wakabayashi T. The two actin-binding regions on the myosin heads of cardiac muscle. Biochemistry. 2002; 41:5429–5438. [PubMed: 11969403]

Moczarska A, Kakol I. The influence of regulatory light chains on structural organization of cardiac myosin heads interacting with actin and ATP. BiochemMolBiolInt. 1995; 37:765–772.

Moore JR, Leinwand L, Warshaw DM. Understanding Cardiomyopathy Phenotypes Based on the Functional Impact of Mutations in the Myosin Motor. Circ Res. 2012; 111:375–385. doi:10.1161/circresaha.110.223842. [PubMed: 22821910]

Muthu P, et al. Structural and functional aspects of the myosin essential light chain in cardiac muscle contraction. FASEB J. 2011; 25:4394–4405. doi:http://dx.doi.org/10.1096/fj.11-191973. [PubMed: 21885653]

O'Connell CB, Tyska MJ, Mooseker MS. Myosin at work: Motor adaptations for a variety of cellular functions. Biochim Biophys Acta. 2007; 1773:615–630. [PubMed: 16904206]

Palmiter KA, Tyska MJ, Dupuis DE, Alpert NR, Warshaw DM. Kinetic differences at the single molecule level account for the functional diversity of rabbit cardiac myosin isoforms. J Physiol. 1999; 519:669–678. doi:http://dx.doi.org/10.1111/j.1469-7793.1999.0669n.x. [PubMed: 10457082]

Pant K, Watt J, Greenberg M, Jones M, Szczesna-Cordary D, Moore JR. Removal of the cardiac myosin regulatory light chain increases isometric force production. The FASEB Journal. 2009; 23:3571–3580. [PubMed: 19470801]

Petzhold D, Simsek B, Meißner R, Mahmoodzadeh S, Morano I. Distinct interactions between actin and essential myosin light chain isoforms. Biochem Biophys Res Commun. 2014; 449:284–288. doi:http://dx.doi.org/10.1016/j.bbrc.2014.05.040. [PubMed: 24857983]

Pierce BG, Hourai Y, Weng Z. Accelerating Protein Docking in ZDOCK Using an Advanced 3D Convolution Library. PLoS ONE. 2011; 6:e24657. doi:10.1371/journal.pone.0024657. [PubMed: 21949741]

Plotnikov SV, Millard AC, Campagnola PJ, Mohler WA. Characterization of the Myosin-Based Source for Second-Harmonic Generation from Muscle Sarcomeres. Biophys J. 2006; 90:693–703. [PubMed: 16258040]

Rayment I, et al. Three-dimensional structure of myosin subfragment-1: A molecular motor. Science. 1993; 261:50–58. [PubMed: 8316857]

Rosell FI, Boxer SG. Polarized absorption spectra of green fluorescent protein single crystals: transition dipoles moment directions. Biochemistry. 2003; 42:177–183. [PubMed: 12515552]

Schaub MC, Hefti MA, Zuellig RA, Morano I. Modulation of contractility in human cardiac hypertrophy by myosin essential light chain isoforms. Cardiovasc Res. 1998; 37:381–404. [PubMed: 9614495]

Scruggs SB, Solaro RJ. The significance of regulatory light chain phosphorylation in cardiac physiology. Arch Biochem Biophys. 2011; 510:129–134. [PubMed: 21345328]

Sherwood JJ, Waller GS, Warshaw DM, Lowey S. A point mutation in the regulatory light chain reduces the step size of skeletal muscle myosin. Proc Natl Acad Sci USA. 2004; 101:10973–10978. [PubMed: 15256600]

Siemankowski RF, White HD. Kinetics of the interaction between actin, ADP, and cardiac myosin-S1. J Biol Chem. 1984; 259:5045–5053. [PubMed: 6715335]

Steffen W, Smith D, Simmons R, Sleep J. Mapping the actin filament with myosin. Proc Natl Acad Sci USA. 2001; 98:14949–14954. [PubMed: 11734631]

Stout AL, Axelrod D. Evanescent field excitation of fluorescence by epi-illumination microscopy. Applied Optics. 1989; 28:5237–5242. [PubMed: 20556034]

Sun X, Ekker SC, Shelden EA, Takubo N, Wang Y, Burghardt TP. In vivo orientation of single myosin lever-arms in zebrafish skeletal muscle. Biophys J. 2014; 107:1403–1414. [PubMed: 25229148]

Timson DJ. Fine tuning the myosin motor: the role of the essential light chain in striated muscle myosin. Biochimie. 2003; 85:639–645. [PubMed: 14505818]

Toepfer C, et al. Myosin Regulatory Light Chain (RLC) Phosphorylation Change as a Modulator of Cardiac Muscle Contraction in Disease. J Biol Chem. 2013; 288:13446–13454. doi:http://dx.doi.org/10.1074/jbc.M113.455444. [PubMed: 23530050]

Tokunaga M, Imamoto N, Sakata-Sogawa K. Highly inclined thin illumination enables clear single-molecule imaging in cells. Nature Methods. 2008; 5:159–161. [PubMed: 18176568]

Tyska MJ, Hayes E, Giewat M, Seidman CE, Seidman JG, Warshaw DM. Single-Molecule Mechanics of R403Q Cardiac Myosin Isolated From the Mouse Model of Familial Hypertrophic Cardiomyopathy. Circ Res. 2000; 86:737–744. doi:10.1161/01.res.86.7.737. [PubMed: 10764406]

Wang L, Muthu P, Szczesna-Cordary D, Kawai M. Characterizations of myosin essential light chain's N-terminal truncation mutant Δ43 in transgenic mouse papillary muscles by using tension transients in response to sinusoidal length alterations. J Muscle Res Cell Motil. 2013a; 34:93–105. [PubMed: 23397074]

Wang Y, Ajtai K, Burghardt TP. Qdot labeled actin super-resolution motility assay measures low duty cycle muscle myosin step-size. Biochemistry. 2013b; 52:1611–1621. doi:http://dx.doi.org/10.1021/bi301702p. [PubMed: 23383646]

Wang Y, Ajtai K, Burghardt TP. Analytical comparison of natural and pharmaceutical ventricular myosin activators. Biochemistry. 2014a; 53:5298–5306. doi:http://dx.doi.org/10.1021/bi500730t. [PubMed: 25068717]

Wang Y, Ajtai K, Burghardt TP. Ventricular myosin modifies In vitro step-size when phosphorylated. J Mol Cell Cardiol. 2014b; 72:231–237. [PubMed: 24726887]

Wang Y, Ajtai K, Kazmierczak K, Szczesna-Cordary D, Burghardt TP. Cardiac myosin essential light chain N-terminus regulates motor step-size. Biophys J. 2015; 108:598a. doi:10.1016/j.bpj.2014.11.3252.

Xu X, Meiler SE, Zhong TP, Mohideen M, Crossley DA, Burggren WW, Fishman MC. Cardiomyopathy in zebrafish due to mutation in an alternatively spliced exon of titin. Nat Genet. 2002; 30:205–209. [PubMed: 11788825]

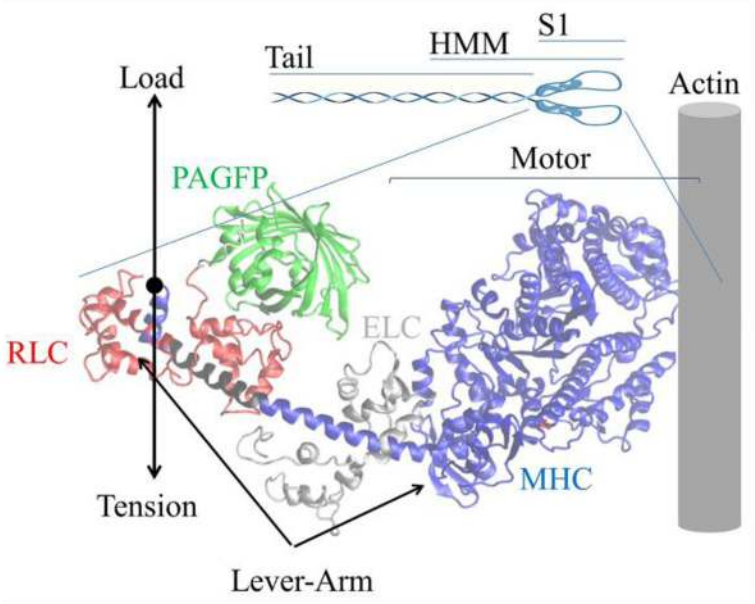

Fig 1.

S1 motor (blue) and lever-arm (blue & black) with bound light chains, ELC (silver) and RLC (red). Photoactivatable GFP (green) linked to RLC is in its known coordination with S1. The full length myosin consists of a tail for filament formation and the S1 ATPase domain. Tryptic digestion of myosin in the presence of Mg produces HMM.

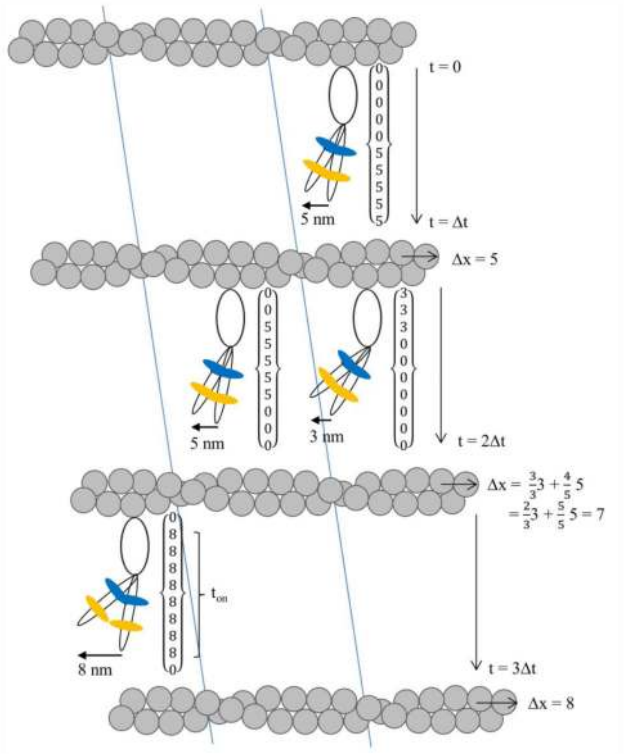

Fig 2.

The time course for actin filament displacement during 4 hypothetical actomyosin interactions. The motor performs 3, 5, or 8 nm unitary steps using different lever-arm movements. Column vectors explicitly indicate the time course with t_{on} the time strongly actin bound. Δx is actin filament displacement in nm.

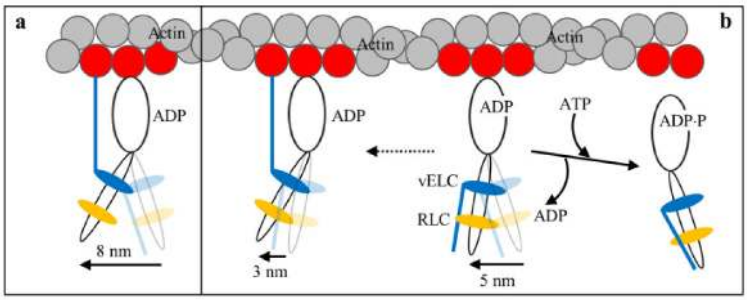

Fig 3.

Proposed 3 step-size mechanism for the βmys power-stroke. **Panel a**: the 8 nm step with the N-terminus of cELC binding. **Panel b**: the 5 nm step (middle) followed by detachment from actin (to right) or an unlikely event with a subsequent 3 nm step (to left). Red actin monomers represent the available myosin binding sites on the filament.

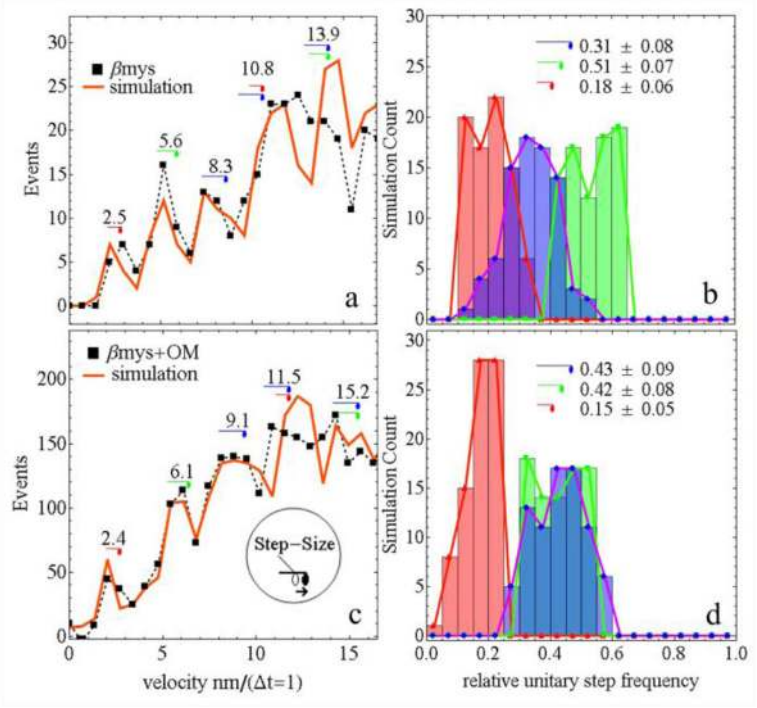

Fig 4.

The Qdot assay velocity event histogram (left) and step-frequency simulation count histogram (right) for the βmys & βmys+OM samples testing the effect of OM on step adaptation in cardiac myosin. Numeric values in **panels a & c** are step-size averages in nm with Δt equal to 0.2 and 0.5 sec for the βmys and βmys+OM samples. Step-size standard deviations are ≤0.6 nm. Numeric values in **panels b & d** are step-frequency averages with standard deviation. Replicates, N, are 6 and 4 for βmys and βmys+OM samples, respectively.

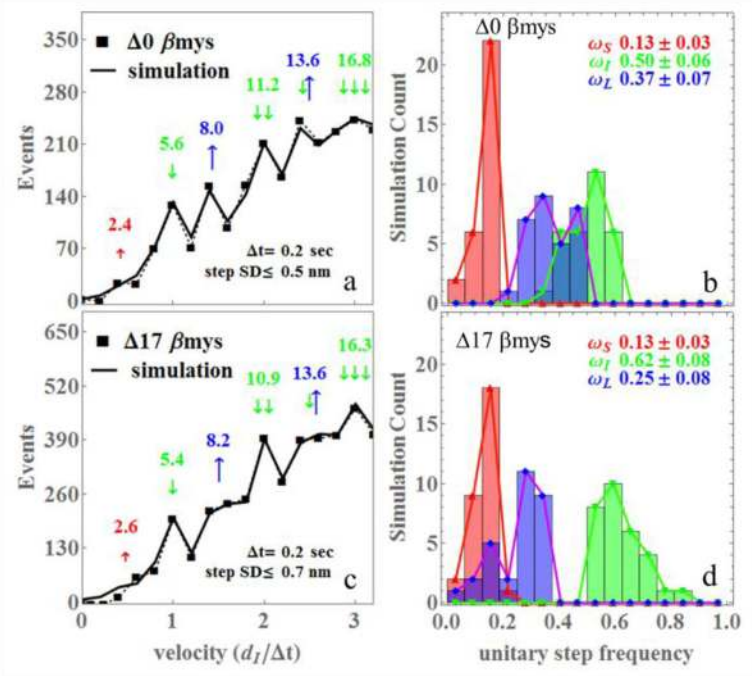

Fig 5.

The Qdot assay velocity-event histogram (left) and step-frequency simulation count histogram (right) for Δ0 (native) and Δ17 βmys constructs. Note the increased single molecule events tabulated in **panel c** compared to the same panel in **Fig 4** and indicating the higher data throughput for the automated assay. Numeric values in **panels a & c** are step-size averages in nm with Δt and standard deviations indicated below the curves. Numeric values in **panels b & d** are step-frequency averages with standard deviation. Replicates, N, are 30-36 for each sample.

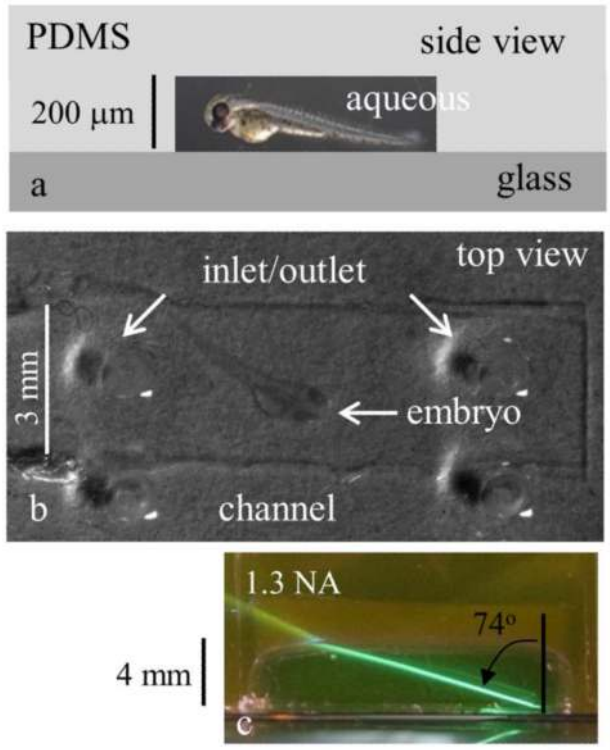

Fig 6.

Panels a & b show the zebrafish embryo confined to a PDMS microfluidic channel 200 μm deep from the side view (**panel a**) and from the top view (**panel b**). **Panel a** is schematic and **panel b** is a photograph of the actual device containing a zebrafish embryo. **Panel c** shows the HILO beam from an oil immersion, 100X, 1.3 NA objective. The beam leaves the glass coverslip at the bottom right and propagates through an aqueous solution containing fluorescein imitating the medium in the embryo confinement microfluidic channel. Emergent beam angle of 74 deg results from an incident angle of ~57.7 deg. A PDMS cube doped with rhodamine B creates he cavity on top of the coverslip. Figure is from (Sun et al. 2014).

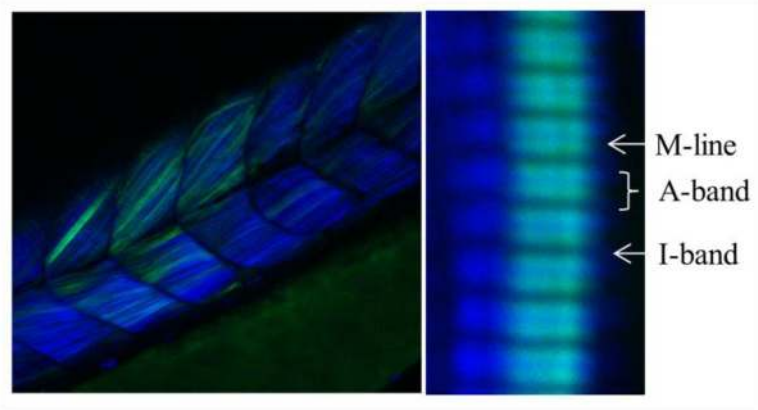

Fig 7.

The left panel shows second harmonic generation (SHG, blue) and fluorescence (green) from RLC-GFP tagged myosin in a zebrafish embryo skeletal truck muscle. SHG indicates the myosin heavy chain. The right panel shows overlap of SHG and fluorescence signals from a single fiber. Exact co-localization of the blue and green bands indicates specific incorporation of the RLC-GFP on myosin. M-line, A-band, and I-band are indicated. Images are from (Sun et al. 2014).

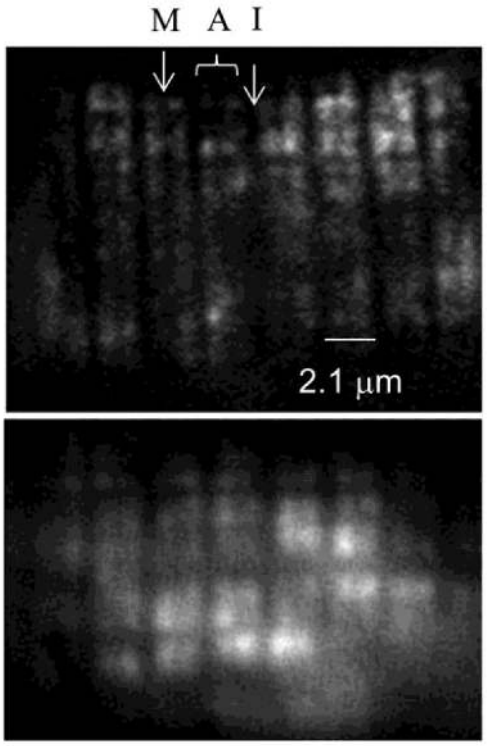

Fig 8.

Photoactivated RLC-PAGFP (top) and RLC-GFP (bottom) tagged embryos under HILO illumination at 488 nm. Photoactivation limits background fluorescence by reducing probability that scattered illumination excites fluorescence from unphotoactivated probes. M-line, A-band, and I-band are indicated. Figure is from (Sun et al. 2014).

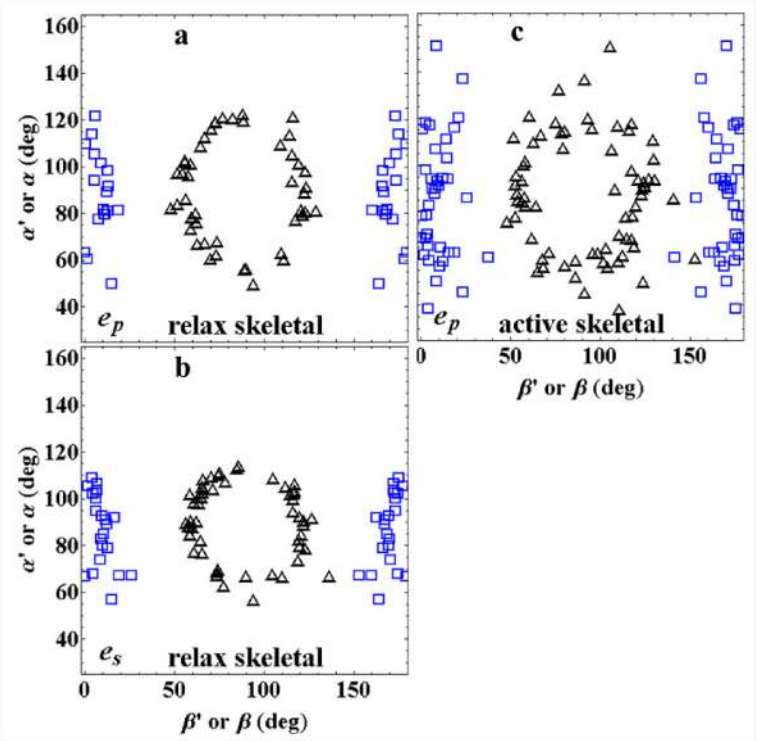

Fig 9.

Probe dipole coordinates (β',α') and indicated by (open triangles) compared to lever-arm helix coordinates (β,α) and indicated by (open squares). Skeletal myosin is from live zebrafish embryos. e_p and e_s indicate p- and s-polarized photoactivating and exciting light polarization.

Table 1

Biochemical/mechanical characteristics of native βmys, RLC S15 phosphorylated βmys (pβmys), and βmys in the presence of OM are compared. Biochemical characterization is the maximum actin-activated ATPase (V_{max}). Unitary mechanical characteristics include: motility velocity (s_m), unitary step-sizes (d) for short (S) intermediate (I) and long (L) steps and their corresponding step-frequencies (co). Ensemble mechanical characteristics include: step-size (<d>) in nm, force (<F>) in arbitrary units (uf), and power (<P>). Errors indicated are standard deviation.

	βmys	**pβmys**	**OM+βmys**
V_{max} (s^{-1})	1.22±0.05	1.26±0.09	1.25±0.08
s_m (μm/s)	0.27±0.02	0.32±0.02	0.039±0.002
d_S (nm)	2.79±0.6	2.8±0.3	2.6±0.6
d_I (nm)	5.39±0.4	4.8±0.3	5.8±0.5
d_L (nm)	7.80±0.6	7.3±0.2	8.8±0.6
ω_S	0.18±0.07	0.15±0.07	0.15±0.06
ω_I	0.51±0.08	0.12±0.08	0.42±0.09
ω_L	0.36±0.09	0.73±0.08	0.43±0.09
<d> (nm)	5.3	6.2	6.6
<F> (uf)	10.1±0.2	15.6±0.2	86±2
<P> (μm/s.uf)	2.7±0.3	5.0±0.4	3.4±0.3